

# 3D-Printed Dielectric Image Lines towards Chip-to-Chip Interconnects for subTHz-Applications

Leonhard Hahn<sup>#1</sup>, Tim Pfahler<sup>#</sup>, Tobias Bader<sup>#</sup>, Gerald Gold<sup>#</sup>, Martin Vossiek<sup>#</sup> and Christian Carlowitz<sup>#</sup>

<sup>#</sup>Institute of Microwaves and Photonics (LHFT), Friedrich-Alexander-Universität Erlangen-Nürnberg

<sup>1</sup>leonhard.hahn@fau.de

**Abstract**— This paper reports on 3D-printed dielectric image lines for low-loss subTHz applications between 140 and 220 GHz. In contrast to conventional dielectric waveguides, a conductive copper substrate is used to achieve robust routing and increased mechanical stability. For easy integration and characterization of the dielectric image line within a waveguide measurement setup, a low-loss mode-converter for flexible mounting is further designed. The characterized overall system exhibits a broadband match of at least 20 dB over the entire frequency band, with minimal losses of below 0.35 dB/cm. Furthermore, multi-line characterization is performed for de-embedding the propagation parameters  $\alpha$  and  $\beta$  of both the dielectric transmission line and the mode-converter, and finally, the influence of discontinuities such as bending radii on the transmission behavior is evaluated. Due to the simplicity of the underlying 3D-printing technology, the proposed concept features extremely low cost and complexity, yet offers high flexibility and outperforms the losses of conventional transmission lines.

**Keywords**— Dielectric image lines, 3D-printing, dielectric waveguide, low-loss transmission lines, subTHz distribution networks

## I. INTRODUCTION

The mmW- and subTHz-domain presents an extremely promising region for further improvement of the performance of modern RF systems. The therefore associated possibility of substantial increase in frequency and bandwidth benefits the resolution capability of imaging radar systems or the data rate of communication systems, therefore motivating the development of a large number of subTHz-capable FMCW systems in recent years [1], [2], [3]. Current investigations clearly indicate the potential and the necessity of those subTHz-FMCW radar applications, especially in the area of high-resolution close-range imaging [4], [5]. However, the transmission loss arising at high frequencies is significant, thus preventing the use of conventional planar transmission lines such as microstrip lines (MSL) or coplanar waveguides (CPW) for signal distribution. Other types of non-planar transmission lines, such as RF cables or hollow waveguides, either don't support the required frequency range any more or have the disadvantage of low flexibility and extremely high manufacturing efforts. Especially in the case of high-performance multi-channel imaging systems with several integrated, but spatially distributed receiver circuits (ICs), the lack of low-loss transmission options is a serious problem due to their equal dependency on mixers in the receive path, which consequently require large distribution networks for feeding every IC with one

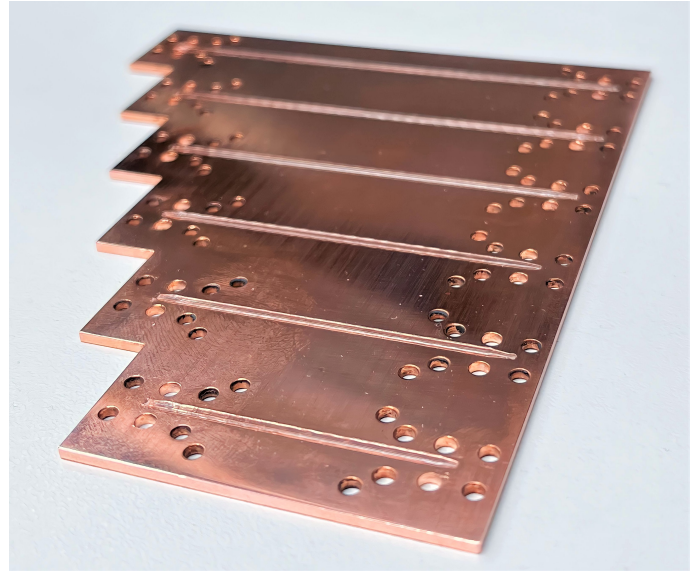


Fig. 1. 3D-printed dielectric image lines on top of a copper substrate.

common local oscillator's signal (LO). Dielectric image lines (DIL) represent one way to realize such subTHz distribution networks. Compared to conventional planar transmission lines, these provide an extremely low-loss [6], hereby enabling the realization of longer, off-chip connections even at subTHz frequencies [7]. In addition to large LO distribution networks, direct chip-to-chip interconnects [8] or on-chip antennas [9] can be created. Furthermore, the possibility of additive manufacturing (3D-printing) makes DILs extremely lightweight, cost-effective and flexible to manufacture [10], which is a significant advantage over extremely expensive RF cables or conventional metallic waveguides. For this reason, dielectric waveguides have recently become a greater focus of study and part of a wide variety of investigations [11], [12], [13]. The DIL is to be understood as a special form of dielectric waveguide, since an additional conductive surface is used in addition to the dielectric [14], see Fig. 1. This serves as an anchor for the DIL, which can be very fragile at high frequency, thus improving the guidance and mechanical stability of the system.

This paper therefore presents exclusively 3D-printed dielectric image lines for G-band applications from 140 GHz up to 220 GHz. Starting from the underlying theory in Section II, the design and fabrication process of both the transmission line and its suitable mode-converter is discussed

in Section III, enabling the connection and use of the DIL in a waveguide system. Finally, Section IV contains the characterization of the resulting overall concept.

## II. IMAGE LINE TOPOLOGY

The basic development of dielectric image lines reaches far back [14], [15] and is to be understood as a modification of the well known conventional dielectric waveguide. Due to its relative permittivity  $\epsilon_r > 1$ , the basic dielectric waveguide (DWG) transfers electromagnetic power with its dominant  $HE_{11}$  mode axially along its dielectric, with radially decreasing electric ( $\vec{E}$ ) and magnetic ( $\vec{H}$ ) field components [10]. Note that in contrast to hollow waveguides, dielectric based waveguides have frequency dependent field components outside their transmission line. For a well-defined polarization state of the guided waves, the DWG geometries are supposed to offer an aspect ratio of  $a/b = 2$  [16], see Fig. 2. DILs are based on the exact same operating principle, but unlike conventional DWGs, they use a conductive sheet as mechanical anchor on their bottom side, enhancing their routing, their mechanical stability and reducing their physical size. In addition, the conducting sheet acts as a polarization anchor, hence simplifies the mode conversion problem by preventing the generation of parasitic modes [14]. To further

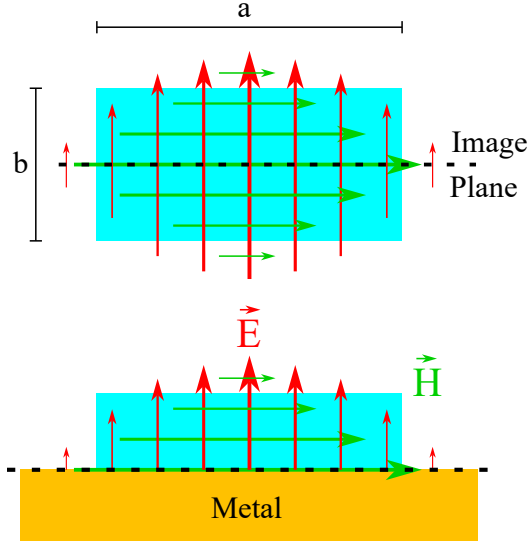


Fig. 2. Electric and magnetic field distribution of a conventional dielectric waveguide (top) and its corresponding image line (bottom).

ensure low-loss propagation of electromagnetic waves, both the electric and magnetic boundary condition of the metal surface ( $E_{\text{tan}} = 0$ ,  $\vec{H}_0 = 0$ ) must comply with the field distribution of the dominant  $HE_{11}$  mode. This is achieved by inserting the metal sheet into the DWG's Y-symmetry plane (image plane), allowing the E- and H-field components to remain unchanged and changing the aspect ratio to  $a/b = 4$ . The resulting field distribution of both the DWG and its corresponding image line can be seen in Fig. 2. In this work, the DIL's dielectric is Cyclic Olefin Copolymer (COC) with a relative permittivity of  $\epsilon_r = 2.2$ . This material is very well

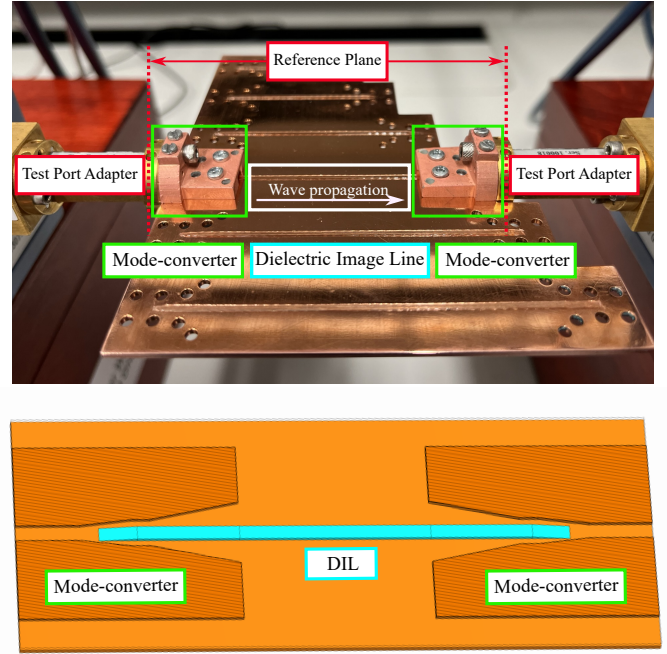


Fig. 3. Measurement setup for the back-to-back characterization of DIL system (top) with sectional view of its schematic (bottom).

suiting due to its low dissipation factor of  $\tan \delta = 1 \cdot 10^{-4}$ , its low water absorption rate and finally its simple 3D-printability with common FDM processes.

## III. MEASUREMENT SETUP

Since the dominant DIL mode  $HE_{11}$  does not occur in any common type of transmission line, the design of a mode-converter is necessary. Key aspect of the design is the possibility to flexibly mount the mode-converter on the upper side of the image surface and thus to excite the DIL, which is lying directly underneath, for subsequent measurements. The mode-converter, like all the DILs, was initially manufactured using 3D-printing technologies, however, a CNC-milled copper version has proven better suitability in respect to mounting precision and is therefore used in this work. To generate the desired signals and feed the mode-converters in the G-band (140 GHz to 220 GHz), the ZVA-Z220 frequency converters from Rohde & Schwarz were used, which are fed by the ZVA24 network analyzer. The DILs are located on the

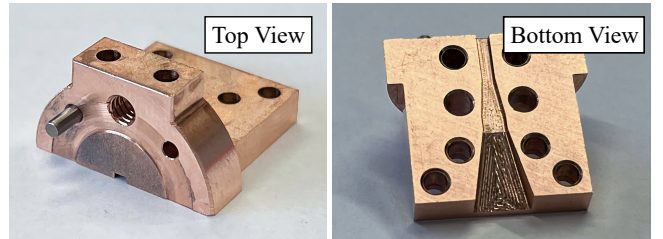


Fig. 4. CNC-milled mode-converter in split-block technology with WR05 waveguide flange for  $HE_{11}$  mode excitation of the 3D-printed DIL.

top of the mirror surface after 3D-printing and connect two mode-converters to form a symmetrical back-to-back setup, so that both reflection- and transmission measurements can be performed to characterize the DILs thoroughly. The schematic concept with mode-converters and DIL as a sectional view is illustrated in Fig. 3, the resulting measurement setup is shown in Fig. 3. After TOSM calibration, the reference plane is located exactly at the mode-converters input, so that a measurement of the entire system is possible. Due to the strong similarity of the injected waveguide mode  $TE_{10}$  to the desired hybrid DIL mode  $HE_{11}$ , the mode-converter only consists of a slightly modified, double-tapered waveguide. After assembly of the mode-converters onto the metal sheet, the printed DILs are located directly in the waveguide channel, see Fig. 4.

The first taper only applies to the width of this waveguide and serves to simplify the subsequent assembly, which otherwise can become challenging due to the similar width-dimensions of DIL and mode-converter's waveguide channel. This conflict worsens with the rather high printing tolerance of the used FDM processes. The second taper includes both the width and the height dimension and thus transforms the waveguide channel into a structure comparable to a horn antenna, which contributes to matching improvements of the DIL. To further enhance matching, the DIL must be designed with a linearly increasing taper of its height. The achievable matching is heavily dependent on the taper length, as can be seen in Fig. 5a). Based on this results, a length of  $l_{\text{taper}} = 3$  mm was chosen. All geometric dimensions of the mode-converter and the DIL have been simulated and optimized for best return loss using electromagnetic field simulations in CST Microwave Studio. This simulations also reveal that compared to other transmission line types, the DIL-topology has a fairly high tolerance for almost all geometric deviations, with the only exception being its initial height tapering.

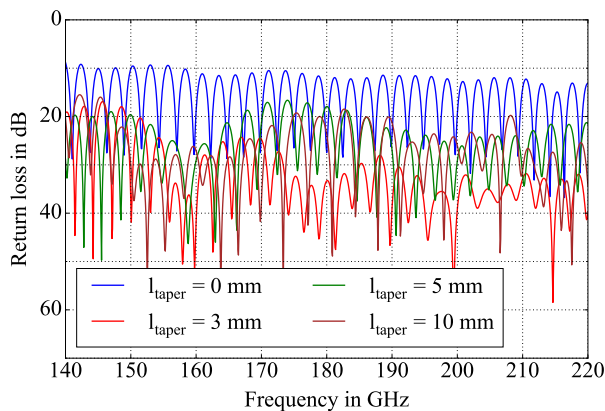


Fig. 5. Influence of the DIL's initial tapering length on their simulated return loss.

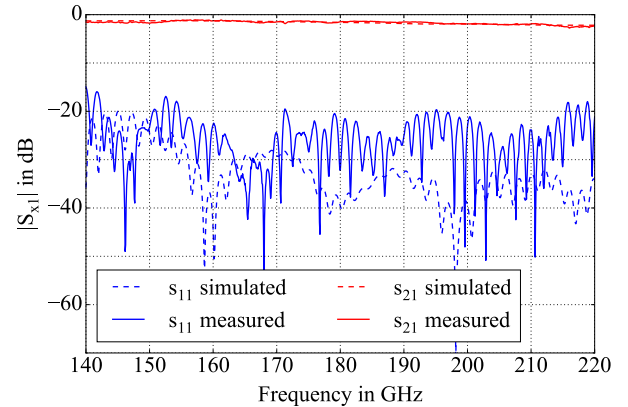


Fig. 6. Simulated and measured S-parameters of a single DIL with length  $l = 60$  mm.

#### IV. RESULTS

For a thorough characterization of the 3D-printed dielectric image lines, S-parameter measurements are performed after the TOSM calibration using the measurement setup presented in Section III. This allows for determination of the transmission- and reflection properties and further investigation of relevant characteristics such as the complex propagation coefficient  $\gamma = \alpha + j\beta$ . Fig. 6 shows the simulated and measured S-parameters for a DIL of length  $l = 60$  mm, the influence of both mode-converters is included. It is clearly evident that the DIL is very well matched over the entire frequency band from 140 GHz to 220 GHz with a return loss (RL) of constantly approx. 20 dB. Furthermore, it exhibits an outstandingly low insertion loss of below 2 dB for frequencies up to 200 GHz, while values of 2.8 dB are still achieved for the maximum frequency of 220 GHz. The measured IL values are in excellent agreement with the simulation data, whereas the RL values deviate slightly from the simulation. This can be explained by the imprecision of the FDM 3D-printing technology,

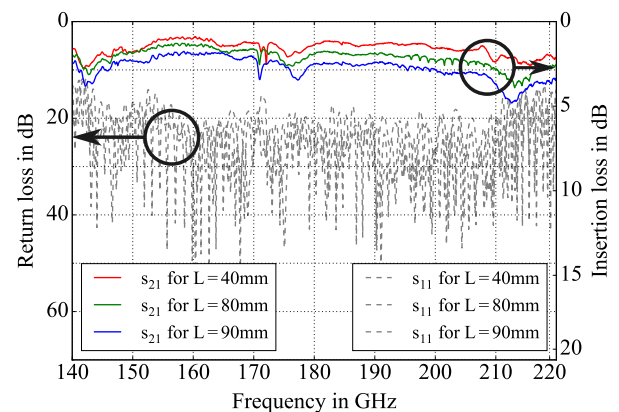


Fig. 7. Measured S-parameters of a multi-line DIL for estimation of the propagation coefficient  $\gamma$ .

which makes precise manufacturing of the DIL's taper very challenging. Deviations in taper length and -structure have a fairly high effect on the return loss of the DILs, as previously shown in Fig. 5. To de-embed the true properties of the transmission lines only, multi-line measurements are performed using DILs of different lengths, between 40 mm and 90 mm). With constant influence of the two mode-converters, the resulting deviations of the  $s_{21}$ -parameters allow the extraction of the propagation coefficient  $\gamma_{\text{DIL}}$ , from which the DIL's attenuation coefficient  $\alpha_{\text{DIL}}$  and phase coefficient  $\beta_{\text{DIL}}$  can easily be read. Fig. 7 exemplarily shows the resulting return- and insertion loss of the multi-line measurement for DILs of three different lengths. As expected, the rise of measured insertion loss is clearly evident with increasing line length, while the measured return loss remains independent of length.

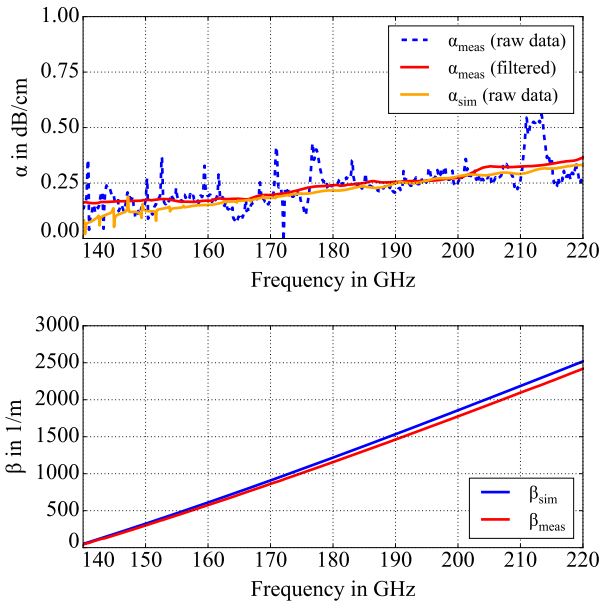


Fig. 8. Determination of the DIL's and propagation parameters  $\alpha$  and  $\beta$  with extraction of the mode-converters's influence on the transmission behavior.

For the subsequent estimation of the attenuation- ( $\alpha$ ) and phase coefficient ( $\beta$ ), see Fig. 8, only the IL results of 2 different lengths are required and used. Therefore, a more thorough de-embedding technique based on all S-Parameter's eigenvalues is performed, enabling possible matching effects to be also taken into account and to be compensated for. The 3D-printed DILs show excellent consistency with a very low average attenuation of only  $0.25 \frac{\text{dB}}{\text{cm}}$ , making them suitable for low-loss transmission applications in the subTHz-domain. Due to the dielectric loss of the DIL and both ohmic loss and roughness of the copper surface,  $\alpha$  is consistently rising, to values around  $0.35 \frac{\text{dB}}{\text{cm}}$  at 220 GHz. The measured results and simulated expectations match in excellent accuracy, with only minor deviations in the 140 GHz range. The phase coefficient  $\beta$  shows an absolutely linear characteristic, which excludes phase distortions. The small deviation from the simulated

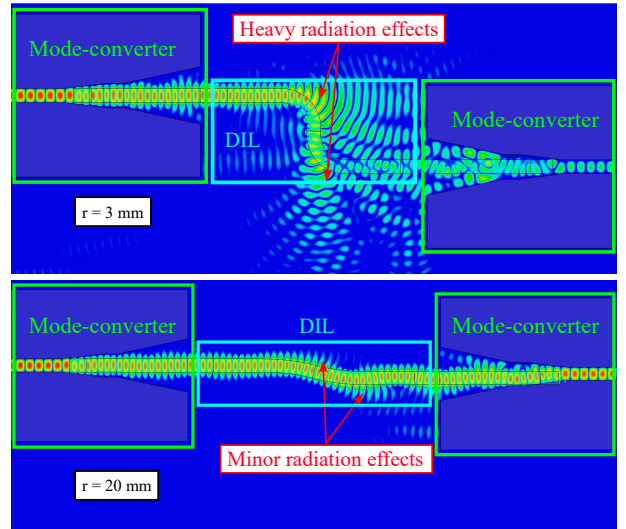


Fig. 9. CST simulation of the field distribution for a 200 GHz excitation of DILs with narrow ( $r = 3 \text{ mm}$ , top) and wide ( $r = 20 \text{ mm}$ , bottom) bending radii, leading to variably strong parasitic radiation.

$\beta$ -value is caused by false assumption of the true effective permittivity value  $\epsilon_{r,\text{meas}} < \epsilon_{r,\text{sim}}$ . After determination of  $\alpha_{\text{DIL}}$ , the corresponding attenuation factor of the mode-converter is assessable. For an excitation of 200 GHz,  $\alpha_{\text{mc}}$  of one single mode-converter is only approx. 0.3 dB, therefore the mode-converter can also be considered low-loss and has only minor influence on the measurement results.

Finally, since the characterized DILs will form the basis for complex dielectric networks and are to be used for subTHz interconnects that are not exclusively running straight, the influence of line discontinuities such as bending radii has to be investigated. As described in earlier fundamentals [11], basically all types of discontinuities represent a sudden impedance variation for a dielectric waveguide, which interrupts the tight field binding and results in radiation at the location of the discontinuity, thus an increasing insertion loss can be expected. Fig. 9 shows the simulated field

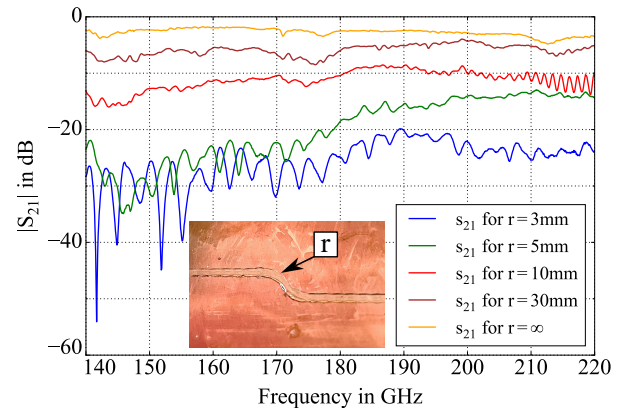


Fig. 10. Radii dependent measured insertion loss due to parasitic radiation effects at line discontinuities of DILs.

distribution for a 200 GHz excitation of two DILs with differing bending radii. For a narrow radius  $r = 3$  mm, the abrupt change of direction leads to heavy parasitic radiation at both corners. For a more gradual radius  $r = 20$  mm, only minor radiation effects are detected, therefore making this value much more suitable for line bends. For verification of this behavior, four DILs with differing bending radii are additively manufactured and characterized with the previously presented measurement setup, see Fig. 10. From the measured  $s_{21}$ , the radius-dependent insertion loss is clearly evident, which increases substantially for low values and prevents the use of DILs with bending radii  $r < 10$  mm. Radii  $r > 30$  mm show only small deviations from straight lines ( $r = \infty$ ), which means that they cause only a minor increase in the insertion loss and are therefore suitable for the desired low-loss applications. Furthermore, especially for small radii, a strong high-pass response can be observed, which is explained by the fact that the electromagnetic field is only loosely bound to its DIL at low frequencies due to the lower effective permittivity  $\epsilon_{r,\text{eff}}$ , which particularly enhances the radiation effects and therefore the attenuation of those lower frequencies.

## V. CONCLUSION

In this paper, dielectric image lines were additively manufactured by using exclusively 3D-printing FDM technology. A characterization of the transmission properties within a frequency converter setup proves the low-loss characteristic of the manufactured DILs with an average and maximum attenuation value of  $0.25 \frac{\text{dB}}{\text{cm}}$  and  $0.35 \frac{\text{dB}}{\text{cm}}$ , respectively. Moreover, the dielectric transmission line exhibits broadband matching in the entire frequency band from 140 GHz to 220 GHz with a return loss of 20 dB, enabling the use of 3D-printed dielectric image lines for subTHz networks, especially for multi-channel signal distribution in chip-to-chip interconnects or for dielectric on-chip antennas. Feasibility of line bends is given, however, bending radii below 30 mm are to be avoided due to the generation of strong parasitic radiation, that could lead to interference in adjacent components. With reasonable radii values, a compromise between additional insertion loss and flexibility and accessibility of the DIL routing could be reached. Unavoidable deviations of the desired DIL geometry have proven to have only minor impact on the quality of its transmission behavior. On the contrary, multiple tests have demonstrated that especially the initial taper, the accuracy of its mode-converter assembly and finally the surface quality of the underlying image plane are the dominant influence on the achievable transmission quality.

## VI. ACKNOWLEDGEMENT

This work was supported by the German Research Foundation (DFG) within the frame of the research project TeraCaT (funding code 1519-54792 7558172). The authors would also like to thank particularly the institutes' mechanics department, namely Kurt Hack and Jürgen Popp, for the precise fabrication of all necessary tools and assemblies.

## REFERENCES

- [1] X. Yi, C. Wang, M. Lu, J. Wang, J. Grajal, and R. Han, "4.8 a terahertz fmcw comb radar in 65nm cmos with 100ghz bandwidth," in *2020 IEEE International Solid-State Circuits Conference - (ISSCC)*. IEEE, 2020, pp. 90–92.
- [2] C. Mangiavillano, A. Kaineder, K. Aufinger, and A. Stelzer, "A 1.42-mm 2 0.45–0.49 thz monostatic fmcw radar transceiver in 90-nm sige bicmos," *IEEE Transactions on Terahertz Science and Technology*, vol. 12, no. 6, pp. 592–602, 2022.
- [3] K. Statnikov, E. Ojefors, J. Grzyb, P. Chevalier, and U. R. Pfeiffer, "A 0.32 thz fmcw radar system based on low-cost lens-integrated sige hbt front-ends," in *2013 Proceedings of the ESSCIRC (ESSCIRC)*. IEEE, 2013, pp. 81–84.
- [4] D. Jasteh, M. Gashinova, E. G. Hoare, T.-Y. Tran, N. Clarke, and M. Cherniakov, "Low-thz imaging radar for outdoor applications," in *2015 16th International Radar Symposium (IRS)*. IEEE, 2015, pp. 203–208.
- [5] S. Gu, G. Xi, L. Ge, Z. Yang, Y. Wang, W. Chen, and Z. Yu, "Compressed sensing for thz fmcw radar 3d imaging," *Complexity*, vol. 2021, pp. 1–10, 2021.
- [6] D. D. King and S. P. Schlesinger, "Losses in dielectric image lines," *IEEE Transactions on Microwave Theory and Techniques*, vol. 5, no. 1, pp. 31–35, 1957.
- [7] Y. Torabi, G. Dadashzadeh, M. Hadeie, H. Oraizi, and A. Lalbakhsh, "A wide-angle scanning sub-terahertz leaky-wave antenna based on a multilayer dielectric image waveguide," *Electronics*, vol. 10, no. 17, p. 2172, 2021.
- [8] J. W. Holloway, L. Boglione, T. M. Hancock, and R. Han, "A fully integrated broadband sub-mmwave chip-to-chip interconnect," *IEEE Transactions on Microwave Theory and Techniques*, vol. 65, no. 7, pp. 2373–2386, 2017.
- [9] H. Tesmer, D. Stumpf, E. Polat, D. Wang, and R. Jakoby, "Dielectric image line rod antenna array with integrated power divider at w-band," in *2022 16th European Conference on Antennas and Propagation (EuCAP)*. IEEE, 2022, pp. 1–5.
- [10] F. Distler, M. Sippel, J. Schur, G. Gold, K. Helmreich, and M. Vossiek, "Additively manufactured dielectric waveguides for advanced concepts for millimeter-wave interconnects," *IEEE Transactions on Microwave Theory and Techniques*, vol. 67, no. 11, pp. 4298–4307, 2019.
- [11] F. Distler, J. Schur, and M. Vossiek, "In-depth characterization of a dielectric waveguide for mmw transmission line applications," in *2018 IEEE 22nd Workshop on Signal and Power Integrity (SPI)*. IEEE, 2018, pp. 1–4.
- [12] S. Fukuda, Y. Hino, S. Ohashi, T. Takeda, H. Yamagishi, S. Shinke, K. Komori, M. Uno, Y. Akiyama, K. Kawasaki, and A. Hajimiri, "A 12.5+12.5 gb/s full-duplex plastic waveguide interconnect," *IEEE Journal of Solid-State Circuits*, vol. 46, no. 12, pp. 3113–3125, 2011.
- [13] M. Geiger, M. Hitzler, S. Saulig, J. Iberle, P. Hugler, and C. Waldschmidt, "A 160-ghz radar with flexible antenna used as a sniffer probe," *IEEE Sensors Journal*, vol. 17, no. 16, pp. 5104–5111, 2017.
- [14] D. D. King and S. P. Schlesinger, "Dielectric image lines," *IEEE Transactions on Microwave Theory and Techniques*, vol. 6, no. 3, pp. 291–299, 1958.
- [15] K. Solbach and I. Wolff, "The electromagnetic fields and the phase constants of dielectric image lines," *IEEE Transactions on Microwave Theory and Techniques*, vol. 26, no. 4, pp. 266–274, 1978.
- [16] A. Hofmann, E. Horster, J. Weinzierl, L.-P. Schmidt, and H. Brand, "Flexible low-loss dielectric waveguides for thz frequencies with transitions to metal waveguides," in *33rd European Microwave Conference, 2003*. IEEE, 2003, pp. 955–958.